State-to-state rate constants for the collisional interaction of Xe($7p$), Xe($6p'$), and Kr($5p'$) atoms with He and Ar

G. Zikratov and D. W. Setser
Department of Chemistry, Kansas State University, Manhattan, Kansas 66506

(Received 2 August 1995; accepted 3 November 1995)

One-photon laser excitation of Xe($6s[3/2]_2$) and Kr($5s[3/2]_2$) atoms that were generated in a discharge-flow reactor was used to study the collisional relaxation of the Kr($5p'[3/2]_1$, $[3/2]_2$, and $[1/2]_1$), the Xe($7p[3/2]_2$, $[3/2]_1$, $[5/2]_2$, and $[5/2]_3$), and the Xe($6p'[3/2]_1$, $[3/2]_2$, and $[1/2]_1$) states in He and Ar. Both cw and pulsed laser excitation techniques were utilized to obtain the total deactivation rate constants and product formation rate constants at 300 K. Collisions with He mainly produce Xe* and Kr* product states with small energy defects, but the rate constants can be as large as 20×10^{-10} cm^3 atom^{-1} s^{-1}, which correspond to thermally averaged cross sections of 150 Å^2. Because of the rapid collisional coupling of populations in nearly isoenergetic levels, multicomponent exponential decay of the initially produced state is frequently observed. The deactivation rate constants for Ar are smaller than for He, but the product distributions tend to be more diverse than for He, and arguments based only on energy defects are not necessarily a good guide to the favored product state(s) from Ar collisions. The magnitude of the quenching cross sections for Ar is consistent with the crossing of an entrance channel with several diabatic exit channel potentials. However, the superlarge quenching cross sections for Xe*–He to just one or two product levels require special considerations. The Kr($5p'$) and Xe($6p'$ and $7p$) rate constants with He are discussed with respect to collisional effects upon the use of cw optical pumping to convert populations in the metastable Xe($6s[3/2]_2$) and Kr($5s[3/2]_2$) levels to the Xe($6s'[1/2]_0$) and Kr($[5s'[1/2]_0$) levels. © *1996 American Institute of Physics.* [S0021-9606(96)02406-1]

I. INTRODUCTION

Collisional relaxation by He and Ar of Xe* states within the $6p'$, $7p$, and $6d$ manifolds (88 000–90 000 cm^{-1}) has been studied by pulsed and cw one-photon, laser-induced fluorescence (LIF) following excitation from the Xe($6s[3/2]_2$) state; the metastable atom concentration was generated in a flowing–afterglow reactor. Our immediate interest was to understand the difficulty of generating a Xe($6s'[1/2]_0$) metastable atom concentration from the reservoir of Xe($6s[3/2]_2$) atoms using optical pumping via the Xe($6p'[1/2]_1$) level in He or Ar carrier gases.[1] However, understanding the energy relaxation mechanisms for the excited levels of Xe is of practical importance for modeling the kinetic processes in discharge devices, such as excimer lasers[2] and the Xe atomic laser.[3] Several of these Xe* Rydberg levels have been used for resonance enhanced multiphoton generation of laser beams in the VUV and extreme UV regions,[4] and collisional processes can be important in these experiments because Xe can be used along with another rare gas to reduce the phase mismatch at large detuning from the atomic resonance.[4] The Xe* energy levels of interest are given in Fig. 1; the Racah notation will be used to label the states. Some cw LIF experiments involving the Kr($5p'$) levels (shown in Fig. 2) in He and Ar also will be described. These experiments were done because of our interest in converting the population in the Kr($5s[3/2]_2$) level to the Kr($5s'[1/2]_0$) level by optical pumping via the Kr($5p'[3/2]_1$) state.[5] The rate constants for deactivation of the Kr($5p'$) states in He and Ar are needed to understand collisional loss of populations from the intermediate state.

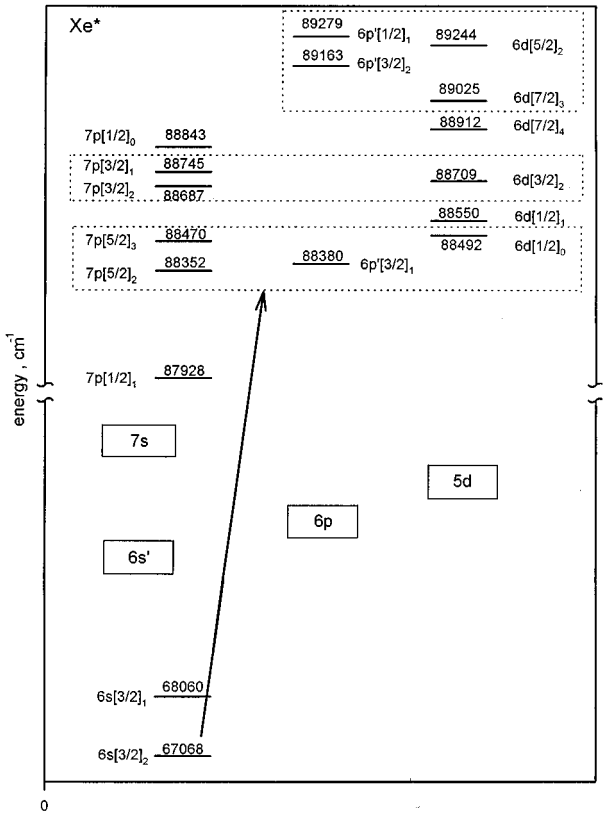

FIG. 1. Diagram showing the Xe($7p$, $6p'$; and $6d$) states, which are identified by the Racah notation. The number in the square bracket is the vector sum of the angular momentum of the Xe^+ core and the orbital angular momentum of the Rydberg electron; the subscript is the total angular momentum, J. The dashed boxes enclose the three sets of levels that are strongly coupled by He collisions.

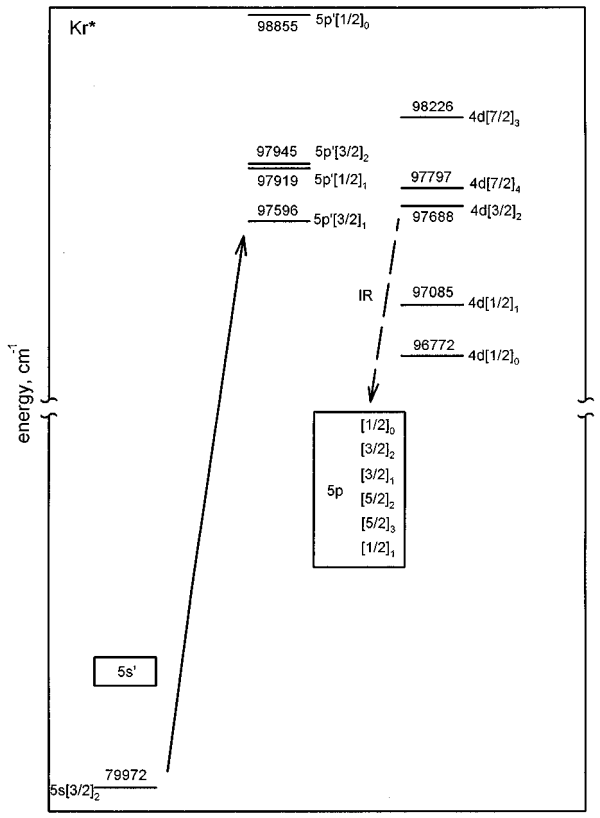

FIG. 2. Diagram showing the Kr($5p$, $4d$, and $5p'$) states. The dashed arrow shows the radiative decay pathway for the collisionally populated Kr($4d$) states formed by collisions. The Kr($4d$) states have radiative lifetime 100–150 ns; Kr($4d[7/2]_4$) radiates only to Kr($5p[5/2]_3$); Kr($4d[7/2]_3$) radiates only to $5p[5/2]_2$ (~0.86) and $5p[5/2]_3$ (~0.14); Kr($4d[3/2]_2$) radiates mainly to $5p[1/2]_1$ (~0.48) and $5p[3/2]_2$ (~0.42) and weakly to $5p[5/2]_2$ (~0.04) and $5p[3/2]_1$ (~0.06). The Kr($5p$) states were identified by observation of the $5p \rightarrow 6s$ fluorescence, see text.

The collisional relaxation mechanism for states of the Xe($6p$) manifold (77 000–80 000 cm^{-1}) has been studied experimentally [6–8] and theoretically[9] for all rare gas atoms as collision partners, because of interest in the atomic Xe laser,[3] which operates on transitions between levels of the $5d$ and $6p$ manifolds. Large quenching rates of the Xe($6p[3/2]_1$) level were shown to be responsible for the increase in laser gain at the 2.03 μm transition of the atomic Xe laser with added He.[3(a)] Details of the formation and collisional relaxation of the upper Xe($5d$) laser levels are not completely understood, but they are thought to be generated mainly by electron recombination with $ArXe^+$.[3(e),3(f)] Although individual Xe($6p$) levels have different rate constants, the general magnitudes are 1×10^{-10} cm^3/s for Xe, 1×10^{-11} cm^3/s for Kr and Ar, 1×10^{-12} cm^3/s for He, and 10^{-13} cm^3/s for Ne.[8] Experiments and *ab initio* calculations[9] both show a dependence of the rate constants on the specific initial and final levels and on the collisional partner, because of the sensitivity to the interactions between the diabatic potentials.

The pulsed one-photon LIF technique from the Xe($6s[3/2]_2$) level previously was used in this laboratory to study relaxation within the Xe($7p$ and $6p'$) manifolds and intermultiplet transfer to the Xe($6d$) states in Ne and Ar, but no data were taken for He.[10] The relaxation between states of the $6p'$, $7p$, and $6d$ manifolds has also been studied by two-photon excitation of the $J=0$ and 2 states from the ground state of Xe in Ar, Kr, and Xe buffer gases.[7(b),7(c),11] Rate constants for the Xe($6p'$ and $7p$) states are usually larger than for Xe($6p$), and they are approximately 5×10^{-10} cm^3/s in Xe, 4×10^{-10} cm^3/s in Kr, and 3×10^{-10} cm^3/s in Ar and Ne.[7(b),7(c),11] Rapid collisional coupling among Xe($6p',6d,7p$) states with small energy defects in He was suspected as one cause of the low efficiency for transfer of population from Xe($6s[3/2]_2$) to Xe($6s'[1/2]_0$) via optical pumping of Xe($6p'[1/2]_1$). On the other hand, optical pumping to the Xe($7p[5/2]_3$) level followed by collisional transfer to the Xe($6p'[3/2]_1$) level was more successful.[1] The present study provides an explanation in terms of the collisional coupling mechanisms. We have found unusually large cross sections, ~150 $Å^2$, in He for collisional transfer between levels of Xe* with energy separation of 20–30 cm^{-1}. Such large cross sections require coupling of potential curves at distances of about 10 Å and provide the opportunity to study mechanisms of nearly resonant energy exchange between levels that are not coupled by dipole selection rules.

An advantage of the one-photon excitation technique from Xe($6s[3/2]_2$) and Kr($5s[3/2]_2$) states in a flow reactor is the very low concentration of Kr or Xe, thus only collisions with atoms of the carrier gas need to be considered in analysis of the data. Also, complications from amplified stimulated emission[12] (ASE) of the Xe($6p'$ and $7p$) states are absent. Both ASE and collisions with the parent gas (0.2–2.0 Torr) plus collisions with the added reagent must be considered for pulsed two-photon laser excitation of Xe($6p'$ and $7p$) from the ground state atoms.[11,12] On the other hand, Kr and Xe are too expensive to be used as carrier gases and two-photon experiments in static cells are required to study collisions of Xe($6p',7p$) with Xe or Kr.[7,11]

II. EXPERIMENTAL METHODS

The experiments were done in discharge-flow reactors, see Fig. 3, using cw and pulsed LIF measurements. The reactor for the cw experiments has been discussed in previous papers describing optical pumping to generate Kr($5s'[1/2]_0$) or Xe($6s'[1/2]_0$) concentrations starting from the $[3/2]_2$ metastable states generated by a low current dc discharge.[1,5,13] Two cylindrical Ta-foil electrodes (2 cm in length and 1 cm in diameter) separated by 2 cm were placed inside a 1.2 cm diameter glass tube. A dc discharge of 150–400 V generated the metastable atoms. The buffer gas flow in the tube was maintained by a Pfeiffer Balzers mechanical pump with booster. About 2 cm downstream from the discharge, the tube turns to form a Wood's horn light trap and connects to a larger tube, which serves as the laser cell [see Fig. 3(a)]. The LIF observation zone was ~20 cm downstream from the discharge. The average flow speed was about 300 m/s in the main reactor. This discharge-flow reac-

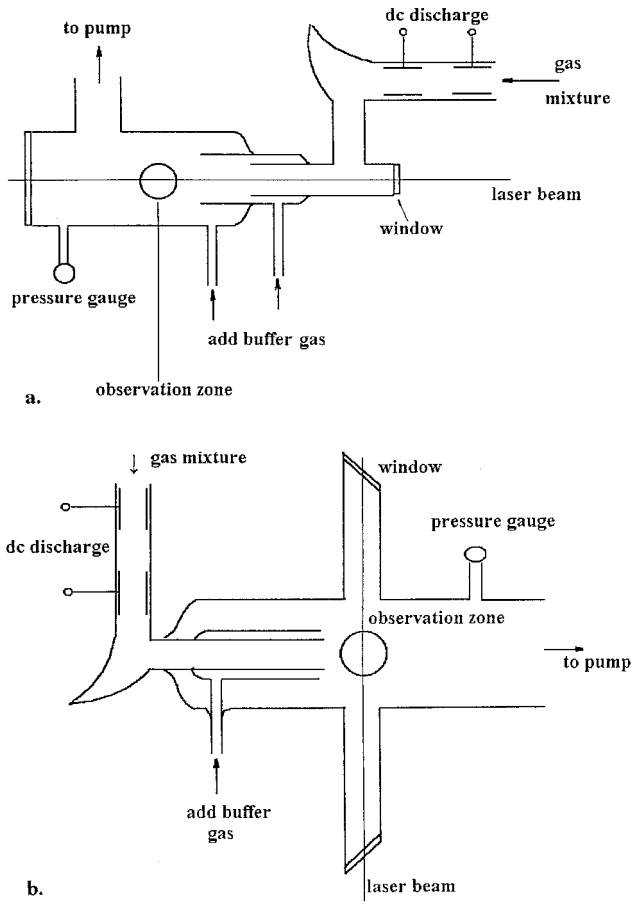

FIG. 3. (a) Schematic drawing showing the flow reactor for the cw LIF experiments. (b) Schematic drawing showing the flow reactor for the pulsed LIF experiments.

tor generates a $Xe(6s[3/2]_2)$ concentration of about 10^{10} atoms/cm^3 from a 1/100 Xe/He mixture at pressures of 0.3–1.0 Torr. The metastable concentration at the observation zone decreases markedly for lower pressures because of rapid diffusion to walls with subsequent quenching.[13] Technical grade He and Ar were purified by passing the gases through traps cooled with liquid nitrogen or dry ice (for Ar); research grade Xe and Kr (99.995% Cryogenic Rare Gases) were used without further purification. The pressure of the buffer gas could be changed by passing more gas through the discharge or by adding it directly to the laser-induced fluorescence zone.

A tunable dye laser pumped by an Ar-ion laser (Coherent model Innova 100–200 UV) was used for the cw experiments. The bandwidth for operation with a birefringent filter is about 40 GHz, which is larger than the Doppler and hyperfine broadened atomic lines of Xe and Kr.[1,5] The power of the cw laser was 20–30 mW; however, a neutral density filter was used to reduce the laser intensity by a factor of 10 for the LIF experiments to avoid significant depletion of the $[3/2]_2$ state. The laser beam was directed along the gas flow with the plane of polarization parallel to the monochromator slit. The fluorescence was dispersed by a 0.3 m McPherson monochromator, which viewed the fluorescence perpendicular to the laser beam. The monochromator had 1200 l/mm gratings blazed at 300 or 1000 nm and a Hamamatsu 955 photomultiplier tube (PMT). The wavelength response of the system was calibrated with a standard halogen-tungsten lamp in the region from 300 to 850 nm. Another recording system (monochromator with a PMT) placed on the opposite side of the flow recorded the intensity of one of the LIF lines as a monitor to the stability of the cw laser. Photon counting was used to record the signals from the PM tubes.

The discharge-flow reactor for the pulsed experiments was almost the same as for the cw experiments [see Fig. 3(b)]; however, the pulsed dye laser beam was directed across the gas flow. The slit of the monochromator was aligned with the laser beam. To eliminate any possible ambiguity in conversion from atomic line intensities to the relative populations of the levels, the plane of the linear polarized laser beam was set at an angle of 54° (magic angle),[14] so that the fluorescence is independent of the m_J populations, i.e., even if the quenching and depolarization[6] cross sections are similar, the initial polarization of the fluorescence will not affect the data. The energy of the dye laser pulse was ~1 mJ and the full width at half maximum (FWHM) pulse width was 9 ns. Most of the $Xe(6s[3/2]_2 \rightarrow 6p',7p)$ transitions were saturated at this power. The laser system was the Nd-YAG pumped dye laser (Quanta Ray) described previously.[6] The time and wavelength resolved fluorescence from the individual Xe (parent as well as product) levels was recorded with the same monochromator and PMT as in the cw experiments. The wave forms from 1024 pulses were averaged by a digital storage oscilloscope (Hewlett Packard 54522A) and transferred to a PC for analysis.

III. EXPERIMENTAL RESULTS

A. Methods of analysis

After a Xe or Kr atom is excited, a number of processes can occur. The atom can spontaneously radiate to lower levels with probabilities that are products of the branching ratios and the total Einstein coefficient,[8,10,15] it can undergo stimulated emission back to the initial metastable state, and it can change state by collision with the carrier gas atoms. Collisions with reactive species such as He or Ar metastables, atomic ions, dimer ions, or thermal electrons can also change the state, but these processes have negligible importance in our experiments because of the low concentrations of these species in the fluorescence zone. This was demonstrated in two ways. First, the carrier gas (He or Ar) was added before and after the discharge. The shapes and the relative intensities of the wave forms were the same in both cases, which proves that only the He ground state concentration changes the populations of the levels. Second, the dc voltage was changed from 150 to 310 V at a constant pressure of He (1.0 Torr) to alter the current through the discharge from 1 to ~10 mA. If thermal electrons were responsible for mixing of the Xe states, then changes in the waveforms should be observed. However, no changes were noticed. The partial pressures of Xe or Kr were two orders of magnitude lower than

that of the carrier gas. The pressure of He or Ar was varied from 0.2 to 2.0 Torr to measure the collisional rate constants of these buffer gases.

The results from the cw experiments are the relative populations of the states in question and how they change with pressure. The ratio of the intensities (the quantities measured in the experiments) from two excited levels (i and j) is proportional to the concentrations with the coefficient of proportionality being the ratio of the Einstein coefficients of the two transitions

$$\frac{I_{ik}}{I_{jl}}=\frac{A_{ik}[\mathrm{Rg}(i)]}{A_{jl}[\mathrm{Rg}(j)]},$$

where I is the fluorescence intensity corrected for response of the detector and A is the Einstein coefficient for the state-to-state transition. This relationship is correct only in the absence of stimulated emission. Therefore, precautions were made to ensure that the laser intensity was low enough so that stimulated emission was negligible.

Consider processes that occur for three excited states (i, j, and k) that are related in the following way: Rg(i) is the initially prepared state, Rg(j and k) are products, and Rg(l) is a lower level to which Rg(i, j, and k) are coupled radiatively:

$$\mathrm{Rg}(i)\rightarrow\mathrm{Rg}(l)+h\nu_{il}, \tag{1a}$$

$$\mathrm{Rg}(i)+\mathrm{He}\rightarrow\mathrm{Rg}(j)+\mathrm{He}, \tag{1b}$$

$$\mathrm{Rg}(j)+\mathrm{He}\rightarrow\mathrm{Rg}(k)+\mathrm{He}, \tag{1c}$$

$$\mathrm{Rg}(j)\rightarrow\mathrm{Rg}(l)+h\nu_{jl}, \tag{1d}$$

$$\mathrm{Rg}(k)\rightarrow\mathrm{Rg}(l)+h\nu_{kl}. \tag{1e}$$

However, Rg(i, j, and k) can be converted into each other by a secondary collision. The ratio of the population of the initial state (i) and a primary product state (j) can be obtained from steady-state analysis for [Rg(j)], and is given by

$$\frac{[\mathrm{Rg}(j)]}{[\mathrm{Rg}(i)]}=\frac{k_{ij}[\mathrm{He}]}{\Sigma_k k_{jk}[\mathrm{He}]+\Sigma_l A_{jl}}. \tag{2}$$

The rate constant for the primary process, Eq. (1b), is k_{ij}, the rate constants for the secondary process, Eq. (1c), are k_{jk} and A_{jl} are the Einstein coefficients for radiative decay. The reverse processes for Eqs. (1b) and (1c) are neglected. Equation (2) can be simplified at low pressures, since $\Sigma_l A_{jl}\gg\Sigma_k k_{jk}[\mathrm{He}]$, and the simple Stern–Volmer equation is obtained:

$$\frac{[\mathrm{Rg}(j)]}{[\mathrm{Rg}(i)]}=\frac{k_{ij}[\mathrm{He}]}{\Sigma_l A_{jl}}. \tag{3}$$

The $\Sigma_l A_{jl}$ is the inverse of the radiative lifetime. The lifetimes and radiative branching ratios for the Xe and Kr states are known.[8,10,15] If secondary collisions are important, the Stern–Volmer plots will become curved as shown by Eq. (2). The lifetimes are 50–100 ns for most of the Xe* and Kr* states of interest. If the rate constants are 10×10^{-10} cm^3/s, the He or Ar pressure must be less than ~0.5 Torr to avoid effects of secondary collisions.

For states formed by two consecutive steps, the steady-state expressions must include both steps and the explicit expressions are complicated. In the low pressure limit, the loss of population from the intermediate state due to collisions is negligible, and the ratio of the product and parent populations is simply a product of the ratios for the two steps. For an $i\rightarrow j\rightarrow n$ process where $i\rightarrow j$ is collisional and $j\rightarrow n$ is radiative, the low pressure limiting ratio is

$$\frac{[R(n)]}{[R(i)]}=\frac{k_{ij}[\mathrm{He}]}{\Sigma_l A_{jl}}\cdot\frac{A_{jn}}{\Sigma_l A_{nl}}. \tag{4}$$

This equation subsequently will be used to identify collisions with Kr($5p'$) states that give Kr($4d$) states, which radiate to Kr($5p$) and are observed via Kr($5p\rightarrow5s$) fluorescence.

The principal results of the pulsed experiments are relative populations of the parent and product states vs time. Poor signal-to-noise ratios at low pressures limited experiments to He pressures >0.3 Torr. In pulsed experiments, the decay rate of the initially excited state usually is used to extract the total decay rate constant. We observed double and triple exponential decays for several initially prepared levels, indicating rapid collisional coupling to levels with energy defects of $<kT$. Assignment of rate constants from direct analysis of such decay profiles is difficult; therefore, we fitted the time dependence of the product state concentrations to obtain state-to-state rate constants. The fitting was done by integrated the coupled differential rate equations with selected rate constants to reproduce the experimental wave forms of initial and product states. A FORTRAN code based on the rational extrapolation method of Bulrisch and Stoer[16] was used for numerical integration of the coupled equations. The formation and decay rates during the laser pulse were taken into account by including a Gaussian shape of the laser time profile into the rate equation. The results of numerical integration with a specific set of rate constants were compared to the experimental results at three pressures. Particular attention was devoted to the shape of the waveforms rather than relative amplitudes because of possible uncertainties in the conversion from intensities to populations due to uncertain branching ratios for weak transitions.[15] Combining the pulsed and cw data is useful, because the relative intensity data from product states are more reliable from cw experiments, but the dependence of the product populations on time is needed to separate primary and secondary processes.

B. cw experiments from the Kr($5s[3/2]_2$) state

Collisional relaxation of the three lowest states in the Kr($5p'$) manifold was studied, see Fig. 2. The $5p'[1/2]_1$ and $5p'[3/2]_2$ levels are separated by only 26 cm^{-1}. In addition to intramultiplet relaxation, the $4d([3/2]_2$, $[7/2]_3$ and $[7/2]_4)$ levels are likely products. Emission from $5p'[1/2]_1$, $5p'[3/2]_1$ and $5p'[3/2]_2$ to the $5s'$ levels can be observed at 780–840 nm, and the relative populations of these levels were directly monitored. The $4d$ states radiate to the $5p$ states in the infrared (1533–3342 nm, which cannot be detected in our experiments) with lifetimes of ~106–150 ns. However, the population in the $4d$ manifold can be observed

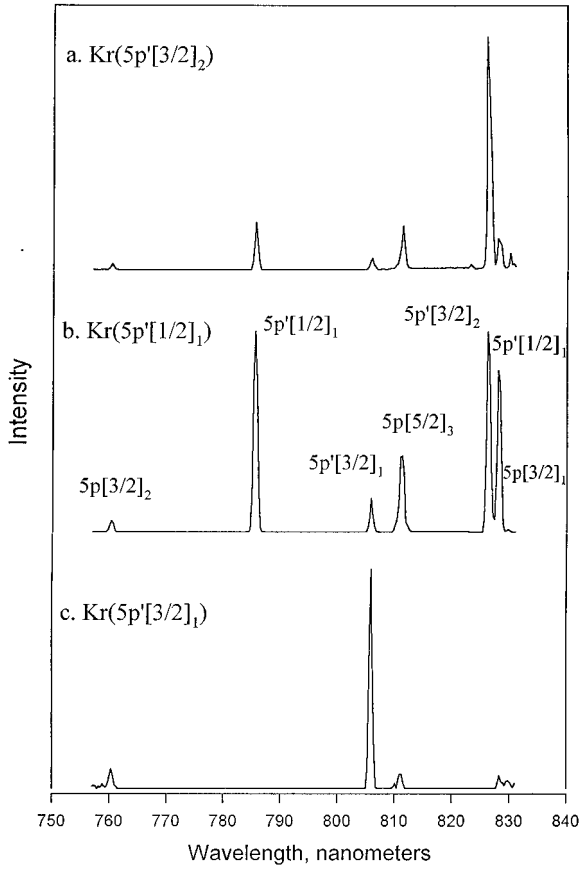

FIG. 4. LIF spectra in 1.5 Torr of He with 5 mTorr Kr for excitation of (a) Kr($5p'[3/2]_2$); (b) Kr($5p'[1/2]_1$); (c) Kr($5p'[3/2]_1$). The labels identify the upper states for the emission lines.

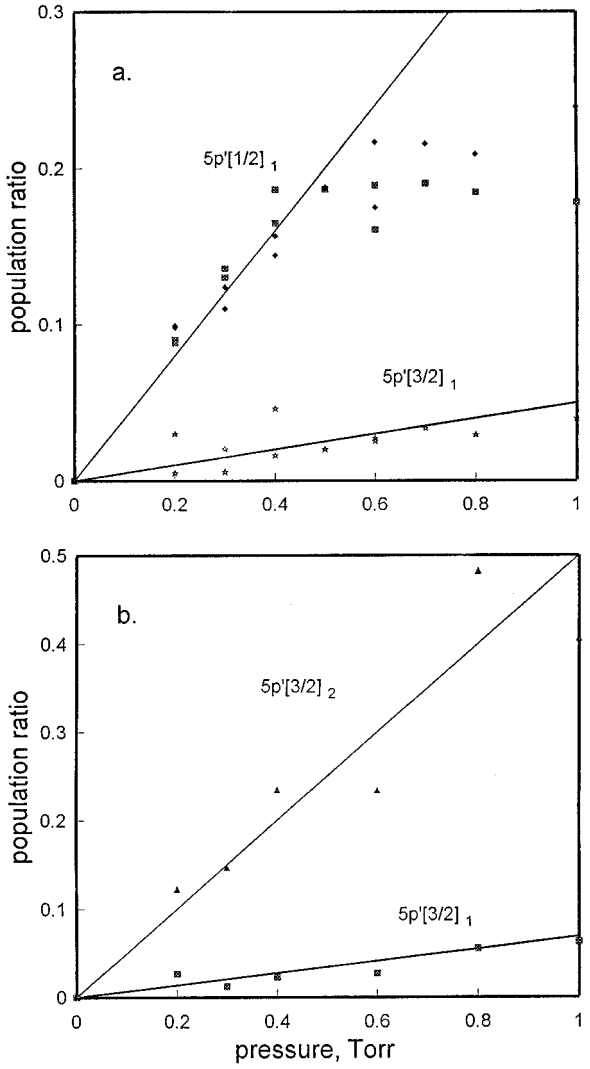

FIG. 5. Stern–Volmer plots of population ratios in He for excitation of (a) Kr($5p'[3/2]_2$) and (b) Kr($5p'[1/2]_1$). The labels show the primary product states for which the population ratio is plotted. The lines are least-square fits to the points. Only points below 0.5 Torr were considered for the linear fit to the Kr($5p'[1/2]_1$) data.

indirectly by transitions from the $5p$ states. The lifetimes of the Kr($5p$) states are ~28 ns, and these states are not mixed by collisions at our pressures.[17] This indirect method for observing Kr($4d$) formation is not ideal, but the data can provide the ratio of intermultiplet vs intramultiplet rate constants for Kr($5p'$) levels, because direct collisional transfer from Kr($5p'$) to Kr($5p$) does not occur in Ar.[17] Although experiments for Kr($5p'$) in He have not been previously done, direct formation of Kr($5p$) is not expected because the Kr($5p'$)–He potentials are not attractive. Since the lifetimes of the Kr($4d$) states are 100–150 ns, which is longer than those of the Kr($5p'$) states, secondary transfer within the $4d$ manifold cannot be avoided. Still, some state specific data were obtained for low pressures of He. For example, the $5p[3/2]_2$ state is formed mainly from $4d[3/2]_2$, the $5p[5/2]_2$ is formed from $4d[7/2]_3$, and $5p[5/2]_3$ is formed from $4d[7/2]_4$ (see the caption of Fig. 2 for branching ratios). Therefore, fluorescence from $5p[3/2]_2$, $5p[5/2]_2$ and $5p[5/2]_3$ was chosen to monitor the $4d[3/2]_2$, $4d[7/2]_3$, and $4d[7/2]_4$ populations, respectively. Since formation of the Kr($5p$) states is a two-step process involving collisional and radiative steps, Eq. (4) was used to relate the relative populations of parent and product states. Collisional transfer into the $4d[1/2]_1$ and $4d[1/2]_0$ levels could not be studied because they radiatively decay to $5p[1/2]_1$, and emission from $5p[1/2]_1$ could not be registered due to the long wavelength. The Kr($5p[3/2]_2$ and $[3/2]_1$) states are formed by excitation-transfer collisions of metastable Ar($4s\ ^3P_2$) atoms with Kr,[18] and strong background emission from these Kr($5p$) levels exist in the reactor even without laser excitation. Therefore, only intramultiplet collisional transfer among the Kr($5p'$) levels could be studied in Ar carrier gas.

A spectrum from excitation of $5p'[3/2]_2$ in He is shown in Fig. 4(a); the main product is the $5p'[1/2]_1$ level, but emission also was observed from $5p'[3/2]_1$ and the Kr($5p$) levels. The $4d[7/2]_4$ state is the most important $4d$ product, as identified by radiation from $5p[5/2]_3$. The formation of $5p[5/2]_3$ via $4d[7/2]_3$ can be ruled out, since the emission intensity from $5p[5/2]_2$, which also would result from $4d[7/2]_3$, was an order of magnitude less than that from $5p[5/2]_3$. The rate constant for collisional transfer to the Kr($4d$) states in He was estimated from the total Kr($5p$)

TABLE I. Collisional rate constants for Kr($5p'$) states in He and Ar.

		k_{ij} (10^{-11} cm^3 s^{-1})		
		cw experiments This work		Pulsed experiments
Parent state	Product state	He	Ar	Ar Ref. 17
$5p'[3/2]_2$	$5p'[1/2]_1$	44± 4	11± 2	10.6±1.0
	$5p'[3/2]_1$	5.5 ± 1	2.2 ± 0.5	
	$4d$ states	33± 8[a]	b	3.6±1.0
	Total observed	83± 12	13±12	14.2±1.2
$5p'[1/2]_1$	$5p'[3/2]_2$	60± 10	22± 3	16.0±1.6
	$5p'[3/2]_1$	8± 1	4.4 ± 0.6	4.1±0.4
	$4d$ states	40±10[a]	b	1 ± 1
	Total observed	110± 20	27± 3	21 ± 2
$5p'[3/2]_1$	$4d$ states	20± 6[c]	d	d
	$5p'[1/2]_1$	1.7 ± 0.2		
	$5p'[3/2]_2$	1.7 ± 0.4		
	Total observed	24± 7		11.4±1.1

[a]The main product series is $4d[7/2]_4$.
[b]The $4d$ states could not be identified in Ar, see text, but the Kr($5p'$) formation constants are nearly equal to the total constant and formation of Kr($4d$) must be minor.
[c]The main product is the $4d[3/2]_2$ state; see text.
[d]Product states could not be observed because of the weak Kr($5p'[3/2]_1 \leftarrow 6s[3/2]_2$) transition and because of background Kr($5p$) emission in Ar.

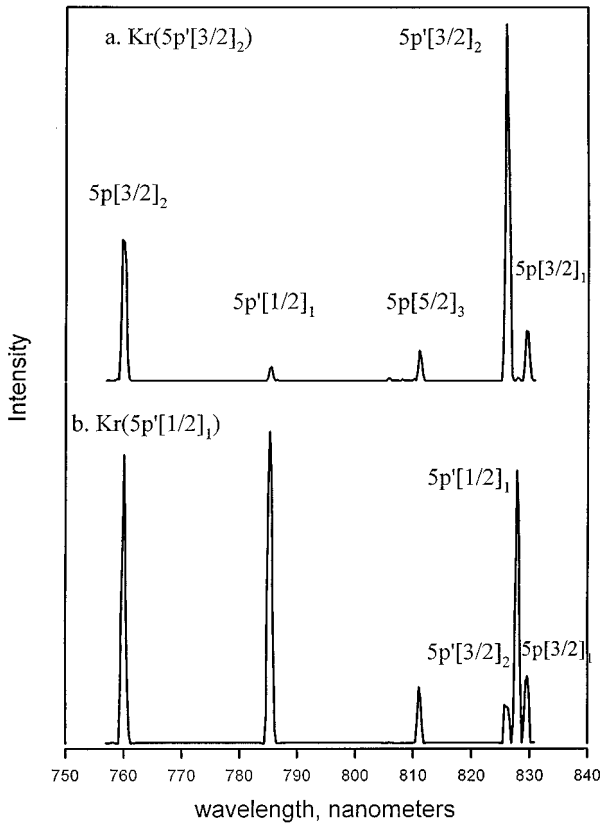

FIG. 6. LIF spectra in 0.6 Torr of Ar with 5 m Torr Kr for cw excitation of (a) Kr($5p'[3/2]_2$) and (b) Kr($5p'[1/2]_1$). The labels identify the upper state of the emission lines.

emission. The situation is similar for excitation of Kr($5p'[1/2]_1$) in He with Kr($5p'[3/2]_2$ and $4d[7/2]_4$) being the main products. The Stern–Volmer plots in Fig. 5 for Kr($5p'[3/2]_2$ and $[1/2]_1$) excitation in He are linear up to 0.5 Torr for products with large constants and to 1.5 Torr for products with smaller ones. The linear fits to the data gave the rate constants in Table I.

As discussed earlier, the Kr($5p$) emission could not be used for identification of Kr($4d$) products in Ar carrier gas. The data for excitation of $5p'[3/2]_2$ and $[1/2]_1$ in Ar (see Fig. 6 for spectra) seem reliable, and the rate constants given in Table I that were assigned from Stern–Volmer plots are in agreement with pulsed experiments.[17] The cw and pulsed data indicate a small rate constant for direct Kr($5p'[3/2]_1$) formation from $5p'[3/2]_2$ and [1/2]. Given the limited number of data points and the fact that the rate constant ratio between Kr($5p'[3/2])_2$ and Kr($5p'[1/2]_1$) gives 2.0 rather than the detailed balance value, 1.5, the smaller $k([1/2]_1 \rightarrow [3/2]_2)$ value from the pulsed experiment is preferred. Based upon the difference between k_{total} from the pulsed experiments and the sum of the rate constants for intramultiplet mixing within Kr($5p'$) levels, the rate constants for $4d[7/2]_4$ formation must be negligible. The data for excitation of both $5p'[3/2]_2$ and $5p'[1/2]_1$ show that the transfer rate to the Kr($4d$) manifold is much less important in Ar than in He.

The data for excitation of $5p'[3/2]_1$ are of poor quality because the transition probability of the $5s[3/2]_2 \rightarrow 5p'[3/2]_1$ absorption is 2 orders lower than for $5s[3/2]_2 \rightarrow 5p'[3/2]_2$. In Ar no Kr* emission could be observed from product states that was above the background given by the Ar($4s[3/2]_2$)+Kr reaction.[18] However, emission was observed [Fig. 4(c)] in He from $5p([5/2]_2$ and $[3/2]_2$), which can be associated with collisional formation of $4d[3/2]_2$; the approximate rate constant is $(15\pm5)\times10^{-11}$ cm^3 s^{-1}. Formation of $4d[7/2]_4$ also occurs since emission from Kr($5p[5/2]_3$) is observed; the rate constant is $\sim 4\times10^{-11}$ cm^3 s^{-1}. Formation of $4d[1/2]_1$ could not be confirmed, because no Kr($5p$) emission could be specifically associated with radiative decay from Kr($4d[1/2]_1$). The pulsed experiments[17] in Ar gave $k_Q = 11.4\times10^{-11}$ cm^3 s^{-1} for Kr($5p'[3/2]_1$), but product states were not identified. These rate constants suggest that the Kr($5p'[3/2]_1$) population will be coupled to the $4d[3/2]_2$ level in He and Ar, subsequent relaxation of the coupled levels to the Kr($4d[1/2]_{0,1}$) states is likely. Thus, the quenching rate constants (now unknown) for the $4d[1/2]_{1,0}$ levels are needed to understand relaxation of the Kr* concentration through the 97 000 cm^{-1} region in both He and Ar buffer gases.

C. Experiments from the Xe($6s[3/2]_2$) state

Continuous wave experiments were done with Xe($6p'[1/2]_1$, $7p[3/2]_2$, and $7p[5/2]_{2,3}$) levels in He and Ar. The laser intensity was not sufficient to excite levels with small oscillator strengths, such as $6s[3/2]_2 \rightarrow 6p'[3/2]_1$ or $\rightarrow 7p[3/2]_1$. The $7p$ and $6p'$ levels radiate to the

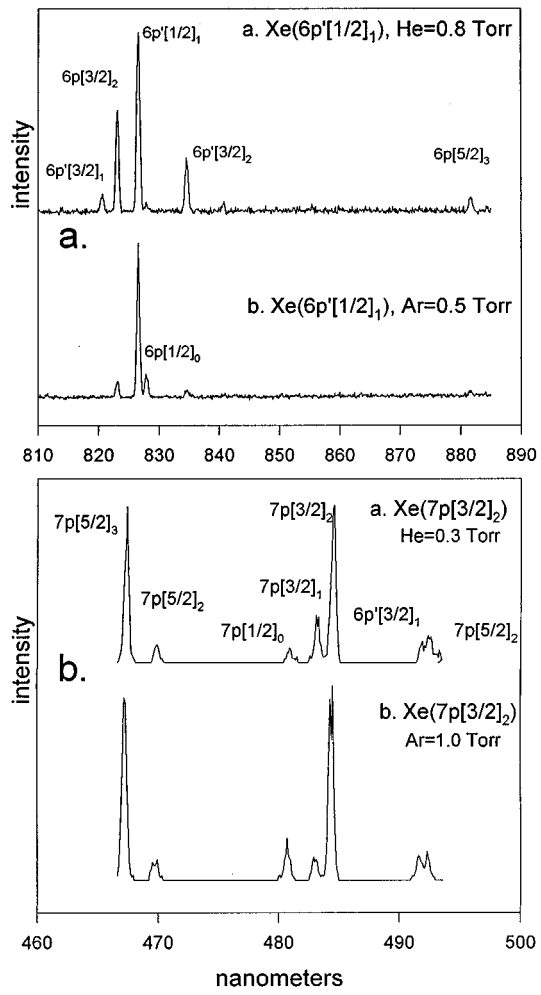

FIG. 7. (a) LIF spectra in (a) 0.8 Torr He and (b) 0.5 Torr Ar for cw excitation of Xe($6p'[1/2]_1$). (b) LIF spectra in (a) 0.3 Torr He and (b) 1.0 Torr Ar for cw excitation of Xe($7p[3/2]_2$). The labels identify the upper state of the emission line.

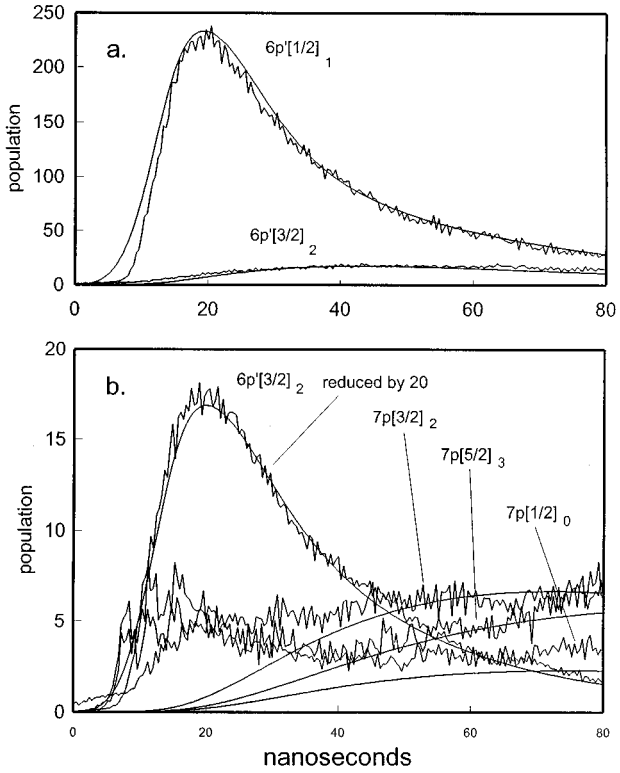

FIG. 8. Time profiles for initially produced and product states for excitation of (a) Xe($6p'[1/2]_1$) and (b) Xe($6p'[3/2]_2$) in 1.0 Torr of He. The states were observed from transitions to the $6s'$ levels. The emission from the product states was weak (note reduction of the initially prepared $6p'[3/2]_2$ concentration by a factor of 20); the scattered laser light (10–30 ns time scale) contributed to the product fluorescence signal for short times. The solid curves are the calculated results.

Xe($6s[3/2]_{1,2}$) states in the 450–490 nm range and to the Xe($6s'[1/2]_{0,1}$) states in the 760–930 nm range. Radiative transitions to the $5d$ and $7s$ manifolds have wavelengths longer than 1100 nm. Since our registration system was limited to <850 nm, and since the response dropped by a factor of 10 from the blue to the red, converting intensities to concentrations from transitions covering a wide range wavelength had some uncertainty. Therefore, data were obtained from either the red or the blue emission; the blue region was usually used because more levels could be observed and the response changed by less than 40% from 450 to 490 nm. For several levels, the Stern–Volmer plots were curved even at low pressure and pulsed experiments were required to identify the mechanism and to assign the rate constants.

Pulsed experiments were performed in 0.3–1.5 Torr of He with the $[1/2]_1$, $[3/2]_1$, $[3/2]_2$, $[5/2]_2$, and $[5/2]_3$ states of the $7p$ manifold and the $[1/2]_1$, $[3/2]_1$, and $[3/2]_2$ states of the $6p'$ manifold to identify the primary and secondary relaxation steps. The decay of the initially excited state and the growth and decay of product levels were measured. Since fast collisional coupling between three or more levels was suspected (and confirmed) for the three sets of levels enclosed in the boxes of Fig. 1, analysis of the multiexponential decay of the parent level was difficult. Fitting the wave forms of the product levels proved to be a more useful way to assign the mechanism and the product formation rate constants. Several sets of data at different pressures provide sufficient information for assignment of the rate constants. The rate constants that fitted the experimental data are summarized in Table II. The uncertainty in the primary rate constants obtained by fitting of the wave forms are 10–15 % for large constants ($\sim 10^{-9}$ cm^3 s^{-1}) and 30–40 % for smaller constants ($\sim 10^{-10}$ cm^3 s^{-1}). The mechanisms for the three sets of strongly coupled levels are considered later. The Xe($6p'$ and $7p$) radiative lifetimes given in Refs. 10(a) and 7(a) were used in the simulations. Since the calculated results matched the experimental low pressure decay rates for which radiative decay is dominant, these radiative lifetimes seem to be reliable.

1. Xe($6p'[1/2]_1$), $6p'[3/2]_2$, and $6d[5/2]_2$)

The spectra in the red region shown in Fig. 7(a) demonstrate that He has a larger quenching rate constant than Ar for $6p'[1/2]_1$ and that Xe($6p$) and Xe($6p'[3/2]_2$) states are products. Weaker emission from $6p'[3/2]_1$ was also ob-

TABLE II. Collisional rate constants for Xe($6p'$,$7p$)+He, Ar.

		k_{ij} (10^{-11} cm^3 s^{-1})				
		cw experiments		Pulsed experiments		
		He	Ar	He	Ar	Ne
Parent state	Product state	This work		This work	Ref. 10[a]	
$6p'[1/2]_1$	$6p'[3/2]_2$	15 ± 3	5 ±1	10 ± 3	0.5±0.3 (4±1)[b]	6.4
	$6d[5/2]_2$	"large"		200 ±30	3.5	
	Total observed		>5 ±1	210 ±30	11±2[b]	29±3
$6p'[3/2]_2$	$6p'[1/2]_1$	8 ± 1[d]		3 ± 1	0.5	0.3
	$6d[7/2]_3^*$			70 ±20		
	$6d[5/2]_2$			20 ± 9	1.9	4.6
	Total observed[a]			93 ±20	16±2	7.0±0.7
$6p'[3/2]_1$	$7p[5/2]_2$	200 ±40[d]		200 ±30	5.2	22
	$7p[5/2]_3$			15 ± 5	1	7
	$7p[3/2]_2$	7 ± 2[d]				
	Total observed	210 ± 40		215 ±35	26±2	37±4
$7p[3/2]_1$	$7p[1/2]_0$			1.0± 0.5		
	$7p[3/2]_2$	60 ±20[d]		40 ±10	0.2	10
	$6d[3/2]_2$			50 ±15	0.2	8
	$7p[5/2]_3$				4.2	
	Total observed[a]			91 ±20	21±2	23±2
$7p[3/2]_2$	$6d[3/2]_2$			180 ±30	7.1	18
	$6p'[3/2]_1$	19 ± 7[c]	4.1 ±0.4			
	$7p[1/2]_0$	4 ± 2	1.6 ±0.1	1.0± 0.5	1.4	0.6
	$7p[3/2]_1$	26 ± 8	3.9 ±0.1	18 ± 6	4.1	2.3
	$7p[5/2]_3$	20 ± 2	5.5 ±0.5	17 ± 6	6.7	
	$7p[5/2]_2$	37 ± 5	3.6 ±0.5	26 ± 7	4.6	
	Total observed[a]	87 ± 26		242 ±50	23±2	21±2
$7p[5/3]_3$	$7p[3/2]_2$	5.0± 0.5		4 ± 1		
	$6p'[3/2]_1$			10 ± 3	4.0	4.0
	$7p[5/2]_2$	13 ± 2		10 ± 3	2.4	2.6
	Total observed[a]	18 ± 3		24 ± 7	24±2	13±2
$7p[5/2]_2$	$7p[3/2]_2$		0.16±0.03	5 ± 1		
	$7p[3/2]_1$		0.3 ±0.1			
	$6p'[3/2]_1$	100 ± 20	0.9 ±0.1	100 ±20	6.7	6.0
	$7p[5/2]_3$	10 ± 1[a]	1.1 ±0.2	8 ± 2	4.3	1.9
	$7p[1/2]_1$		2.6 ±0.4	2.0± 0.5	3.8	0.2
	Total observed[a]	110 ± 20	5.1 ±0.8	119 ±25	24±2	16±2

[a]Total observed is the sum of the individual product formation constants *except* for the last two columns (Ref. 10) for which we list the total quenching constant.
[b]This rate constant was remeasured as $4\pm1\times10^{-11}$ cm^3 s^{-1} using pulsed excitation (see text); the total quenching constant was confirmed to be $11\pm2\times10^{-11}$ cm^3 s^{-1}.
[c]Not a direct process.
[d]Assigned by detailed balance.
[e]The uncertainties for the cw experiments are the least square deviations from the linear plots. The uncertainties for the pulsed experiments are estimates from simulations.

served. The Xe($6p$) states are most likely formed by radiative cascade from the $6d$ levels. The emission from the Xe($6p$) levels, especially $6p[3/2]_2$, is strong even at 0.3 Torr of He and the collisional transfer rate to the $6d(5/2)_2$ level must be very fast, see the following, but the emission pattern from the Xe($6p$) levels was too complicated for detailed analysis. Stern–Volmer plots were made for the $6p'[3/2]_2$ product in He and Ar and the rate constants are given in Table II. The formation rate constant for $6p'[3/2]_2$ in Ar deduced from the cw experiments is 10 times larger than the value assigned from the earlier pulsed work.[10] Therefore, new pulsed experiments in Ar were done to resolve the discrepancy. Pulsed excitation of Xe($6p'[1/2]_1$) with observation of Xe($6p'[3/2]_2$) formation for a range (1–5 Torr) of Ar pressure gave a formation rate constant of $(4\pm1)\times10^{-11}$ cm^3 s^{-1}. The new pulsed data gave a total decay constant of 11×10^{-11} cm^3 s^{-1} and the earlier measurement for k_Q still seems reliable. Formation of $6p'[3/2]_2$, $6d[5/2]_2$, and other $6d$ levels seem to have roughly equal importance in Ar.

Although the cw experiments in He showed emission

from some levels in the $6p$ manifold and from $6p'[3/2]_2$ following excitation of $6p'[1/2]_1$, pulsed experiments showed only very weak emission (it was impossible to record reliable wave forms) from all levels, except the $6p'[3/2]_2$ state. The time dependence of the Xe($6p'[1/2]_1$ and $6p'[3/2]_2$) populations following excitation of the former in 1 Torr of He are shown in Fig. 8(a) along with the simulated curves. The double exponential decay of $6p'[1/2]_1$ is evident, even at 0.25 Torr of He and requires strong coupling ($k=20\pm3\times10^{-10}$ cm^3 s^{-1}) to an intermediate level with a radiative lifetime of about 70 ns. The most likely candidate is the $6d[5/2]_2$ state, which lies 35.5 cm^{-1} below $6p'[1/2]_1$. Emission from $6d[5/2]_2$ could not be observed; however, weak emission from $6p[3/2]_1$ formed in radiative decay from $6d[5/2]_2$ was observed and the rich distribution of Xe($6p$) states observed in the cw experiments is evidence for formation of $6d[5/2]_2$. The formation of $6p'[3/2]_2$ occurs after the coupling between $6p'[1/2]_1$ and $6d[5/2]_2$ is complete. Therefore, transfer from either of these levels to $6p'[3/2]_2$ can occur; however, fitting the $6p'[3/2]_2$ population growth was smoother if transfer from both levels was allowed.

Excitation to $6p'[3/2]_2$ gives emission from the $7p([1/2]_0$, $[3/2]_1$, $[3/2]_2$, and $[5/2]_3)$ levels [see Fig. 8(b)]. A rather large quenching rate constant is required, since the decay time is about 20 ns at 1.0 Torr of He, whereas the radiative lifetime is about 40 ns.[10(a)] Although the wave forms of $6p'[3/2]_2$ appear single exponential up to 1.0 Torr of He, they show a second component with a longer decay (about 70 ns) at higher pressures. Thus, coupling to the $6d$ manifold exists. Unfortunately, transitions from the $6d[7/2]_3$ and $[7/2]_4$ levels are too far in the red to be observed, and the $6d[5/2]_2\rightarrow6p[1/2]_1$ fluorescence is overlapped by the $6p'[3/2]_2\rightarrow6s'[1/2]_1$ transition. A total quenching constant of $9.3\pm2.0\times10^{-10}$ cm^3 s^{-1} was used for the simulated curves in Fig. 8(b). The growth of population in the Xe($7p$) levels is too slow to be associated with this rate constant, because their populations grow after $6p'[3/2]_2$ has decayed. Therefore, the Xe($7p$) product states are formed in a two-step process, and $6d[7/2]_3$ was chosen as the intermediate state. The first stage of the two-step process was simulated with a rate constant of 7.0×10^{-10} cm^3 s^{-1} and the second stage with smaller rate constants of 3.0×10^{-11} cm^3 s^{-1}. The $6p'[3/2]_2$ to $6d[5/2]_2$ transfer rate constant was set as 2×10^{-10} cm^3 s^{-1} to be consistent with the downward rate constant determined from excitation of $6p'[1/2]_1$.

2. Xe($7p[3/2]_1$, $7p[3/2]_2$, and $6d[3/2]_2$

The 460–500 nm spectra from excitation of $7p[3/2]_2$ in He and Ar are shown in Fig. 7(b); emissions from the adjacent levels in the $7p$ manifold and from the $6p'[3/2]_1$ level were observed. However, assignment of the primary vs secondary steps must be done with care, since the $6d[3/2]_2$ level can be involved in the mechanism, which was proven for He by pulsed experiments. The Stern–Volmer plots shown in Fig. 9 for Ar appear linear and direct formation of the $7p[5/2]_{2,3}$ levels seems to be the correct interpretation. The

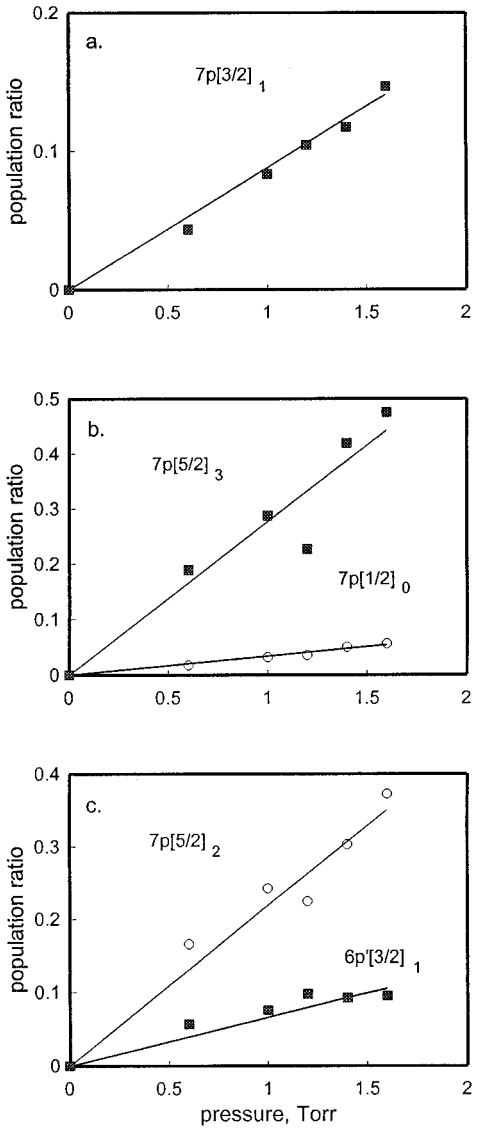

FIG. 9. Stern–Volmer plots of product concentration ratios in Ar for cw excitation of Xe($7p[3/2]_2$). The lines are least-square fits to the data.

Ar data agree with the pulsed experiments[10(a)] to within the experimental uncertainties. The $7p[3/2]_2\rightarrow6d[3/2]_2$ process reported in Ref. 10(a) with a rate constant of 7.1×10^{-11} cm^3/s could not be studied in our cw experiments. Conversely, the collisional transfer to $6p'[3/2]_1$ that we observed was not reported in the pulsed work. These Ar data prove the validity of the cw LIF technique for study of Xe($6p'$,$7p$) states with modest rate constants.

The rate constants for $7p[3/2]_2$ in He are an order of magnitude larger than for Ar, as shown by the product ratios in Fig. 10. Even at 0.2 Torr, the $7p[5/2]_2$, $7p[5/2]_3$, and $7p[3/2]_1$ products have considerable concentrations. The linear plots imply a direct formation mechanism. However, the pulsed experiments prove the existence of an extremely rapid coupling between $7p[3/2]_2$ and $6d[3/2]_2$, and the Xe($7p$) states can be formed from either of the coupled states. The $7p[3/2]_2$ level was easy to excite in pulsed experiments and emission from all levels of the $7p$ manifold and from

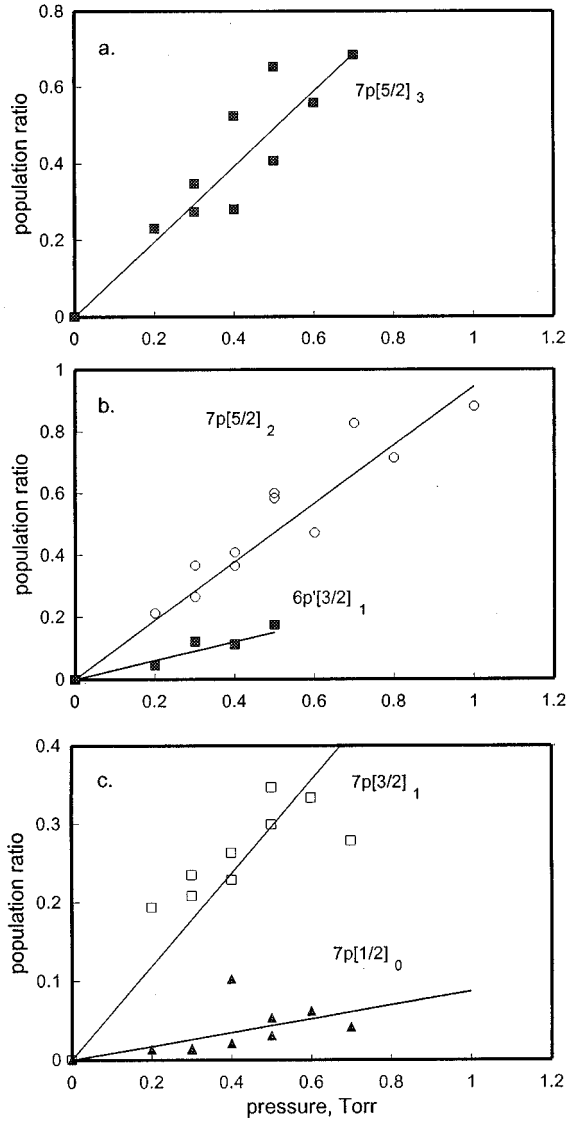

FIG. 10. Stern–Volmer plots of product concentration ratios in He for cw excitation of Xe($7p[3/2]_2$). Straight line are least-square fits to the data. However, the formation of Xe($6p'[3/2]_1$ probably is from a secondary process, see text.

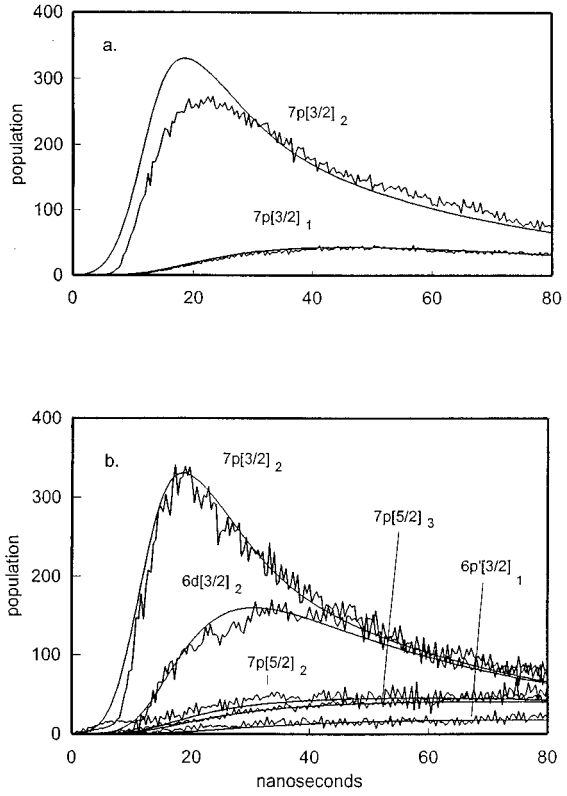

FIG. 11. Time profiles for initially produced and product states for excitation of Xe($7p[3/2]_2$) in 1.0 Torr of He. The solid curves are the calculated results; (a) Experiment showing formation of Xe($7p[3/2]_1$) product, the mismatch between the simulated curve and experimental Xe($7p[3/2]_2$) profile during the laser pulse is probably due to the saturation of the PM tube; (b) Experiment showing formation of Xe($6d[3/2]_2$) (not to scale) as a primary product and Xe($7p$) states as secondary products from Xe($6d[3/2]_2$).

$6p'[3/2]_1$ was observed; also strong emission from $6d[3/2]_2$ was registered in the red. The $6d[3/2]_2$ population grows rapidly, as demonstrated by the experimental and simulated wave forms in Fig. 11(b). The population of $6d[3/2]_2$ is not on the same scale as the others in Fig. 11(b) (because comparison of relative populations from emissions in the blue and in the red was not reliable), but fast growth of the population in this level is demonstrated. From the simulations we conclude that $7p[3/2]_2$ first couples to the $6d[3/2]_2$ level; this is followed by transfer to the $7p[5/2]_{2,3}$ levels. The $7p[1/2]_1$ concentration shown in Fig. 11(a) was fitted by direct transfer with a rate constant of 1.8×10^{-10} cm^3 s^{-1}. The $6p'[3/2]_1$ emission from cw experiments (and pulsed) most likely arises from secondary collision with $7p[5/2]_{2,3}$. The rate constants assigned in Table II from cw and pulsed experiments are self-consistent. The more prominent role of the $6d[3/2]_2$ level in the relaxation mechanism for He relative to Ar should be noted.

The $7p[3/2]_1$ level has a small transition probability, but direct excitation was possible with observation of the growth of $7p[3/2]_2$ emission. The total quenching constant, $(91\pm20)\times10^{-11}$ cm^3 s^{-1}, was divided into 40×10^{-11} for $7p[3/2]_1$ formation and 50×10^{-11} for $6d[3/2]_2$ formation. The simulated decay of $7p[3/2]_1$ matched the experimental results (not shown) at 0.7, 1.0, and 2.0 Torr. The detailed balance rate constant, 18×10^{-11} cm^3 s^{-1}, for $7p[3/2]_1$ formation from $7p[3/2]_2$ matches the experimental result, as shown in Fig. 11(a).

3. Xe($7p[5/2]_2$, $7p[5/2]_3$, $7p[1/2]_1$, and $6p'[3/2]_1$)

The $6p'[3/2]_1$, $7p[5/2]_2$, and $7p[5/2]_3$ levels are especially interesting to us because they were used to collisionally enhance the optical pumping to produce Xe($6s'[1/2]_0$).[1] The 460–500 nm spectra in He and Ar are shown in Fig. 12; emission in the IR region from only $6p'[3/2]_1$, $6p[1/2]_0$, and $6p[3/2]_2$ levels was observed for $\leqslant$1.0 Torr of He. The ratios of the $6p[1/2]_0$ and $6p[3/2]_2$ populations to the $7p[5/2]_2$ population do not change with pressure, which suggests that $6p[1/2]_0$ and $6p[3/2]_2$ are formed mainly in a two-step ra-

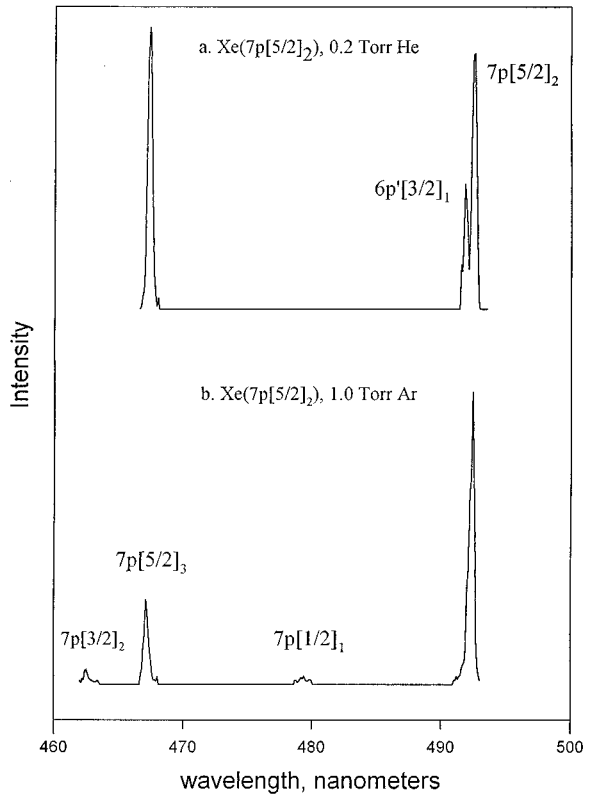

FIG. 12. LIF spectra in (a) 0.2 Torr He and (b) 1.0 Torr Ar for cw excitation of Xe($7p[5/2]_2$).

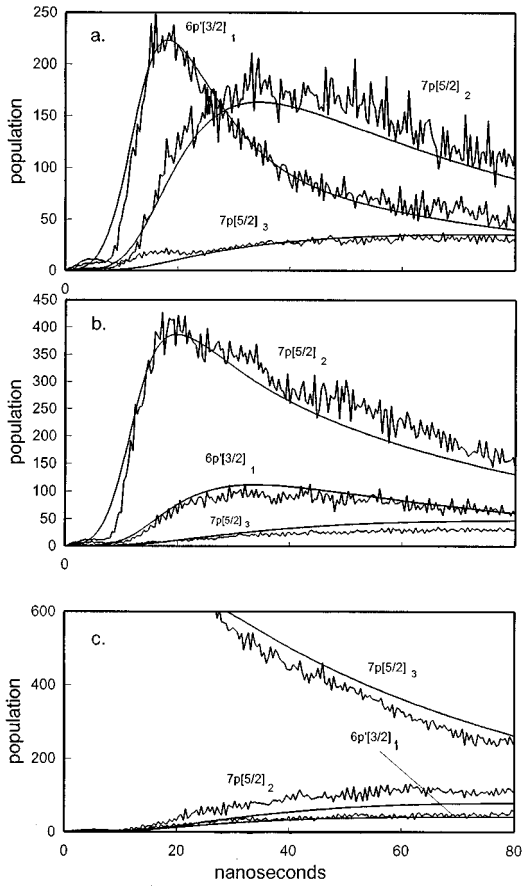

FIG. 13. Time profiles for initially produced and product states for excitation of (a) Xe($6p'[3/2]_1$); (b) Xe($7p[5/2]_2$); (c) Xe($7p[5/2]_3$) in 1.0 Torr of He. The solid curves are calculated profiles for the rate constants in Table II. For excitation of Xe($7p[5/2]_2$), the fluorescence could only be observed after the signal from the scattered laser light had terminated.

diative decay via the $7s$ and $5d$ levels from $7p[5/2]_2$ without collisional transfer. The $6p'[3/2]_1$ population grows very fast with He pressure, and the population ratio becomes constant for pressures $\geqslant$0.5 Torr. Even at 0.2 Torr of He, the $6p'[3/2]_1$ concentration is significant, and the collisional coupling rate between $7p[5/2]_2$ and $6p'[3/2]_1$ is very large. The Stern–Volmer plots were found to curve above $\sim$0.5 Torr of He.

The *observed* product emission for excitation of $7p[5/2]_2$ in Ar corresponds to rather small rate constants and the sum from the Stern–Volmer plots is 5.1×10^{-11} cm^3 s^{-1}, which is much smaller than the total quenching constant, 24×10^{-11} cm^3 s^{-1}, measured from decay times.[10] Product channels corresponding to states that ultimately emit in the red, i.e., the Xe($6d$) or Xe($6s$ and $5d$) states must be important. Similar conclusions were reached from the published pulsed experiments,[10] although an unresolved discrepancy exists for the relative importance of the $6p'[3/2]_1$ product.

The $7p[5/2]_3$ level could be excited and the $7p[3/2]_2$ and $7p[5/2]_2$ products were observed. However, the only observable transition from $7p[5/2]_3$ is back to Xe($6s[3/2]_2$), so Stern–Volmer plots could not be made. From the $7p[5/2]_2$ to $7p[3/2]_3$ rate constant and detailed balance, the rate constant for the reverse process was calculated ($13\pm2\times10^{-11}$ cm^3 s^{-1}) and entered in Table II. The rate constant for $7p[3/2]_2$ formation then was set from the observed relative intensities from $7p[3/2]_2$ and $7p[5/2]_2$ for cw pumping. Experiments in Ar were not attempted.

Pulsed experiments were done to complement the cw data and plots of the relative $6p'[3/2]_1$, $7p[5/2]_2$, and $7p[5/2]_3$ atom concentrations vs time following excitation of the individual levels in 1.0 Torr of He are shown in Fig. 13. The decay of the $6p'[3/2]_1$ concentration, Fig. 13(a), clearly shows two exponential components; the first component lasts about 20 ns. The growth of the population in the $7p[5/2]_2$ level matches the fast decay of $6p'[3/2]_1$, and these two levels reach equilibrium about 25 ns after the laser pulse. This fast coupling could be simulated with a rate constant of $(2.0\pm0.3)\times10^{-9}$ cm^3 s^{-1} for collisional transfer from $6p'[3/2]_1$ to $7p[5/2]_2$. The transfer from the $6p'[3/2]_1$ and $7p[5/2]_2$ levels to the $7p[5/2]_3$ level is much slower. Although it is impossible to decide whether the transfer between $6p'[3/2]_1$ and the $7p[5/2]_3$ occurs directly or via $7p[5/2]_2$, the simulations suggest that a direct channel probably exists from $6p'[3/2]_1$.

Excitation of $7p[5/2]_2$ showed growth of $6p'[3/2]_1$, see Fig. 13(b), confirming the fast collisional coupling between these two levels. Direct transfer from $7p[5/2]_2$ to $7p[5/2]_3$ plus the previously assigned rate constant from $6p'[3/2]_1$ was used to fit experimental profile for $7p[5/2]_3$.

The $7p[5/2]_3$ level is difficult to study directly because

the Einstein coefficients for transitions to lower states are virtually zero, except for the one back to the $6s[3/2]_2$ metastable state (about 39%) and another one to $7s[3/2]_2$ (about 45%) at 3048 nm, far beyond the limit of our apparatus. Since fluorescence from $7p[5/2]_3$ had to be observed at the laser wavelength, only the long term part of the decay could be studied. The decay of the $7p[5/2]_3$ population in Fig. 13(c) is shown starting at 25 ns from the trigger (the delay between the trigger and the laser pulse is due to optical path of the laser beam and the electron transit time of the PMT). Collisional transfer to $6p'[3/2]_1$ and $7p[5/2]_2$ was not as fast as between the $7p[5/2]_2$ and $6p'[3/2]_1$ levels, in accord with the rate constants assigned in the preceding paragraph. Some emission was observed from $7p[3/2]_2$ and a formation rate constant of 4×10^{-11} cm^3 s^{-1} was assigned. We have no knowledge about the possible formation of the $6d[1/2]_{0,1}$ levels, but the $6d[1/2]_0$ level was an important product from $7p[5/2]_3$ in Ne.[10]

Formation of the $7p[1/2]_1$ state was observed from excitation of Xe($7p[5/2]_2$) at $\geqslant$5 Torr of He. Since coupling among the three upper levels is complete at 5 Torr, it is impossible to know which of the three levels gives Xe($7p[1/2]_1$), and we arbitrary assigned the rate constant to $7p[5/2]_2$. The $7p[1/2]_1$ state is separated from $7p[5/2]_2$, $7p[5/2]_3$, and $6p'[3/2]_1$ by more than 400 cm^{-1} and reverse transfer is not important. The rate constant for $7p[1/2]_1$ formation deduced by the rise time following excitation of $7p[5/2]_2$, is $(2.0\pm0.5)\times10^{-11}$ cm^3 s^{-1}.

Although the Einstein coefficient for direct excitation of $7p[1/2]_1$ from $6s[3/2]_2$ is small, we were able to excite and observe fluorescence from $7p[1/2]_1$ for up to 6 Torr He. The radiative lifetime for $7p[1/2]_1$ given by the Stern–Volmer plot was 160 ± 20 ns, which is larger than the (131 ± 4 ns) value measured previously in Ne or in Ar.[10] The Stern–Volmer plot for the first-order decay constants of $7p[1/2]_1$ was of poor quality, so that only an approximate value for the quenching constant, $\sim3\times10^{-12}$ cm^3 s^{-1}, was obtained. This constant must be assigned to formation of $7p[5/2]_2$ to satisfy detailed balance for the reverse process. In fact, formation of $7p[5/2]_2$ was observed, but assigning a formation rate constant from this signal was thwarted by poor signal-to-noise ratio. The decay constant from $7p[1/2]_1$ to lower Xe* states must be $<1\times10^{-12}$ cm^3 s^{-1}. Collisional energy relaxation in the $7p$, $6d$, and $6p'$ manifolds terminates in the $7p[5/2]_2-7p[5/2]_3-6p'[3/2]_1-6d[1/2]_0$ set of levels plus the $7p[1/2]_1$ level. The $7p[1/2]_1$ level will equilibrate with the upper four levels at He pressures of 30 Torr, and radiative decay from the $6p'[3/2]_1$ level serves as a bottleneck to relaxation for $\lesssim$200 Torr of He.

IV. DISCUSSION

A. General aspects of the relaxation pathways for Xe($6p'$,$7p$) and Kr($5p'$) states

We initiated this research in order to understand why conversion of the Xe($6s[3/2]_2$) concentration into the Xe($6s'[1/2]_0$) concentration by optical pumping in a flow reactor was more successful for excitation via the $7p[5/2]_3$ level, rather than the $6p'[1/2]_1$ level. The success for the $7p[5/2]_3$ level depends on several factors: (i) a large Einstein coefficient for the Xe($6s[3/2]_2\rightarrow7p[5/2]_3$) transition with a final state of $J=3$, which forces radiative decay to repopulate Xe($6s[3/2]_2$) exclusively, (ii) collisional transfer of population to the $7p[5/2]_2$ and $6p'[3/2]_1$ levels with a rate in 1 Torr of He that is equivalent to the radiative decay ($\sim$150 ns) of $7p[5/2]_3$, (iii) a favorable radiative branching factor of 0.37 from $6p'[3/2]_1$ to the $6s'[1/2]_0$ level, (iv) rapid coupling of populations in the $7p[5/2]_2$ and $6p'[3/2]_1$ levels, and a 3 times larger radiative decay rate from $6p'[3/2]_1$, than from $7p[5/2]_3$ or $7p[5/2]_2$. The difficulty with optical pumping via the $6p'[1/2]_1$ route is a consequence of (i) an order of magnitude smaller Einstein coefficient, relative to $7p[5/2]_3$, for excitation from Xe($6s[3/2]_2$) and (ii) a collisional transfer rate to the $6d[5/2]_2$ level that matches the radiative decay rate in 0.5 Torr of He. Although, the radiative branching fractions and rates from $6p'[1/2]_1$ and $6p'[3/2]_1$ to Xe($6s'[1/2]_0$) are about the same, collisional transfer of population to the $5d$ manifold from $6p'[1/2]_1$ gives little or no subsequent formation of Xe($6s'[1/2]_0$). In a collision-free environment with a stable laser of adequate power, optical pumping of a population from the Xe($6s[3/2]_2$) state to the Xe($6s'[1/2]_0$) state via the $6p'[1/2]_1$ level should be possible.

The preceding paragraph illustrates the utility of state-to-state rate constants for design of certain applications in rare gases. On the other hand, total relaxation rate constants may be more useful for other needs. In some independent work[11] we have measured the *apparent* single-exponential decay constants following two-photon excitation of the Xe($6p'[3/2]_2$, $7p[5/2]_2$, and $7p[3/2]_2$) states in He. The values are (5.7±0.6), (1.3±0.3), and $(0.12\pm0.02)\times10^{-10}$ cm^3 s^{-1}. The $6p'[3/2]_2$ rate constant is equivalent to the nearly irreversible transfer component to $6d[7/2]_3$. The last two rate constants are approximately equivalent to the effective decay constants from the strongly coupled levels and the numerical values are in general agreement with the sum of the state-to-state rate constants of Table II for transfer out of the sets of levels. The rather slow collisional transfer from the coupled $7p[5/2]_3$, $7p[5/2]_2$, $6p'[3/2]_1$, and, perhaps $6d[1/2]_0$, levels to Xe($7p[1/2]_1$), and the even slower quenching rate from $7p[1/2]_1$, means that these levels act as the bottleneck for collisional loss of population from the Xe($7p$, $6p'$, and $6d$) manifolds in He buffer gas. Although the rate constant for quenching of $7p[1/2]_1$ is larger in Ne,[10(a)] the bottleneck still exists, and the main decay pathway from these levels will be by radiation for up to 20 Torr of Ne and 200 Torr of He. Thus, concentrations can last for a considerable time in the lowest four levels of the Xe($7p$,$6p'$) manifold; the equilibrium $(7p[5/2]_{2,3}+6p'[3/2]_1)/7p[1/2]_1$ concentration ratio is $\sim$2/3. On the other hand, this bottleneck seems not to exist in Ar buffer gas, and the Xe*($6p'$,$7p$,$6d$) populations are collisionally transferred from the lower $7p$ levels into the $7s$ and $5d$ manifolds.

The Kr($5p'[1/2]_1$) level with a radiative lifetime of 26.8 ns and a branching fraction to Kr($5s'[1/2]_0$) of 0.56 was used

as the upper state for pumping the $Kr(5s[3/2]_2)$ concentration to the $Kr(5s'[1/2]_0)$ level.[5] Collisional transfer of population from $Kr(5p'[1/2]_1)$ to either $Kr(5p'[3/2]_2$ or $4d[7/2]_4)$ prevents radiative decay to $Kr(5s'[1/2]_0)$ and reduces the conversion efficiency. The rate constants of Table I give a collisional loss rate in 1 Torr of He of 3.6×10^7 s^{-1}, which is comparable to the radiative decay rate. However, the collisional loss is partly reversible via reexcitation from $Kr(5s[3/2]_2)$, and the optical pumping experiments were successful for $\leqslant$2 Torr of He. The rate constants are smaller in Ar and optical pumping to generate $Kr(5s'[1/2]_0)$ in Ar carrier also is possible.[5]

B. Demkov model for large quenching cross sections of Xe($6p'$,$7p$,$6d$) states in He

Rate constants of 2×10^{-9} cm^3 s^{-1} correspond to thermal cross-sections of 150 $Å^2$ for Xe*+He reactions from $k_Q=\sigma\langle v\rangle$. Such large cross sections cannot be described by the Landau–Zener curve-crossing model, since the potential curves for Xe*–He interactions are virtually flat[9] beyond an internuclear distance of 6 Å (which gives a maximum quenching cross section of $1/2\pi R_x^2=56$ $Å^2$). Other clues about the quenching mechanism is that favored product states have small energy defects, i.e., $\Delta E<kT$, and no selectivity with regard to the angular momentum or ion-core of the initial and product state. This pattern also is found for Ne collisions.[10(a)] However, the cross-sections for $Xe(7p,6p')$ atoms with Ar and Kr (Refs. 7 and 10) are smaller than for Ne or He and the product states are more numerous with larger energy defects. Furthermore, the quenching constants for Ar and Kr are about the same for all $Xe(7p,6p')$ levels. These results for Ar and Kr collisions are consistent with models based upon diabatic curve-crossing formulations.[9] In searching for an explanation for the He and Ne cases, our experimental data were compared to the two-state, semiclassical calculations in the framework of the Demkov model[19] for flat diabatic entrance and exit channel potentials. The Demkov model was developed for quasiresonant, charge-transfer reactions and it is characterized by the internuclear distance, R_0, at which the energy difference between the two potentials is equal to the coupling matrix element between these potentials. The transition between the two states occurs within some region around R_0 with the probability given by[19]

$$P(v,b)=\operatorname{sech}^2\left(\frac{\pi\Delta E}{2(2\ \mathrm{IP})^{1/2}}\left|\frac{dR}{dt}\right|_{R_0}^{-1}\right)\sin^2\left(\frac{1}{h}\int_{-\infty}^{\infty}H_{12}dt\right). \tag{5}$$

The energy difference between the two flat diabatic potentials, ΔE, is equal to the energy difference between the atomic terms at large internuclear distance, IP is the ionization potential for one of the two almost degenerate states, R is the internuclear distance which is time dependent for a collision, and H_{12} is the matrix element for coupling the two potentials. Since the two interacting states are almost degenerate, the coupling term does not have to be large to cause a significant probability. The off-diagonal matrix element is usually taken as the interaction energy between the tails of collisionally perturbed atomic wave functions at large internuclear distances. These terms are rarely available in numerical format from *ab initio* calculations. We used the exchange interaction for atoms with significantly different ionization potentials (such as Xe* and He) as a rough approximation for this energy, since in our estimation we are only interested in R_0.

The internuclear distance in a collision is related to impact parameter, b, and relative velocity, v, as $R=(v^2t^2+b^2)^{1/2}$, where t is the collision time. Since transitions usually occur at large internuclear distances, the integration is over large impact parameters and effective cross sections are large. The time spent by system in the region around R_0 is of crucial importance, as in the Landau–Zener case. Slow collisions allow the system to behave adiabatically, i.e., stay on the original potential and lead to small cross-sections. The

$$\sin^2\left(\frac{1}{h}\int_{-\infty}^{\infty}H_{12}dt\right)$$

term can be replaced by one-half for estimation of the maximum cross sections. To find the distance (R_0) at which $\Delta E=H_{12}$, the coupling matrix element, H_{12}, was taken to be equal to the exchange energy for atom–excited–atom interaction at large internuclear distances.[20(d)] The exchange interaction between two atoms with significantly different ionization potentials was treated in the same way as was previously done for Rydberg states of alkali metal atoms interacting with rare gases.[20] In this treatment, the interaction of the Xe^+ core with the He atom is neglected and the interaction energy, $\Delta(R)$, between the He atom and the Rydberg electron in $l_R=1,m_R=0$ state is approximated by[20(b)]

$$\Delta(R)=\frac{3}{4\beta}\Phi^2(R)\sum_{l=0}^{\infty}(2l+1)C_t. \tag{6}$$

$\Phi(R)$ is the unperturbed radial wave function of the Rydberg electron and l is the ordinal number of spherical harmonics around He sphere. The expressions for the C_l coefficients, which depend on L, the scattering length for the He+ free electron collision, are given by Janev[20(b)] and Smirnov.[20(c)] Basically, Eq. (6) gives the energy shift of all Rydberg levels by $\Delta(R)$ at a given internuclear distance, R. This shift is caused by the presence of the He sphere at the distance R. We assume that when this shift is equal to the energy gap between two unperturbed atomic Rydberg levels they might have an interaction term of approximately the same magnitude. This condition allows us to estimate R_0 used in the Demkov formula [Eq. (5)]. Hydrogen-like wave functions with effective nuclear charges +2.0 and +2.6 for $6p'$ and $7p$, respectively, were used. For an energy defect of 30 cm^{-1}, the $\Delta(R)=H_{12}=30$ cm^{-1} condition is satisfied at $R_0=16$ Å for a $Xe(6p')$ atom and $R_0=27$ Å for a $Xe(7p)$ atom. The integration of $P(b,v)$ over the impact parameter and thermal relative velocity distribution for Xe*+He gives a thermal rate constant of 1.7×10^{-9} cm^3 s^{-1} for $Xe(6p')$ and 2.6×10^{-9} cm^3 s^{-1} for $Xe(7p)$. Although the experimental rate constants do not necessarily show a systematic differ-

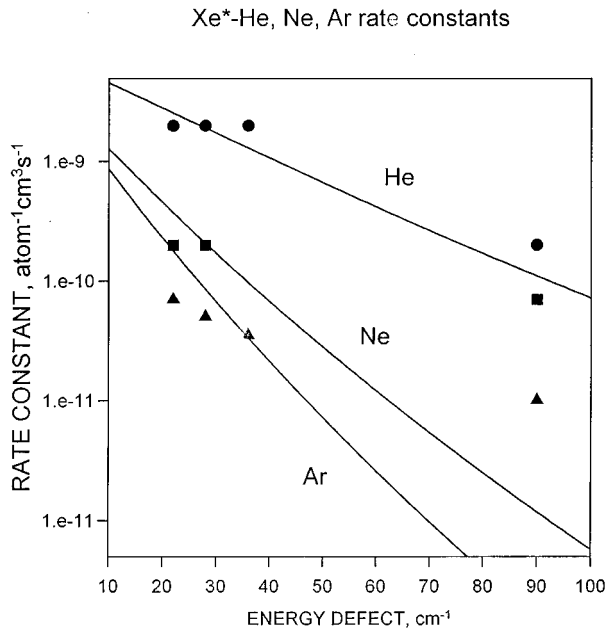

FIG. 14. The dependence of calculated state-to-state rate constants on the energy defects according to the Demkov model in He, Ne, and Ar. The experimental data are (▲) He, (●) Ne, and (■) Ar, for the following pairs of states; $7p[3/2]_2-6d[3/2]_2$, $6p'[3/2]_1-7p[5/2]_2$, $6p'[1/2]_1-6d[5/2]_2$, and $7p[5/2]_3-6p'[3/2]$, listed in order of increasing energy defect.

ence between Xe($6p'$) and Xe($7p$) states, the calculated values are consistent with the magnitude of the large experimental rate constants.

The variation of the calculated 300 K rate constants for Xe($6p'$) with energy defect and mass of the collision partner were investigated for comparison with the data; see Fig. 14. The calculated rate constants for He drop by an order of magnitude as the energy defect increases from 30 to 100 cm^{-1}. The dependence of the rate constants on ΔE is even greater for collisions with Ne and Ar. For a given ΔE, the calculated rate constants decrease with increasing mass of the collision partner. This is a consequence of the smaller thermal velocities for heavier masses. As we mentioned earlier, the probability given by Eq. (5) increases strongly with higher velocity. In fact, for a given velocity the cross sections increase in the order He<Ne<Ar due to the increase in R_0, but this trend is offset in the rate constants by the slower thermal velocities of the heavier atoms. The predicted decrease of the rate constants (for a given energy defect) in the He–Ne–Ar series (see Fig. 14) is generally observed in the experimental data. The dependence on the energy defect also tends to be reproduced, although the fit with the experimental results is not quantitative. Our model is much too general to fit a specific process because, in fact, H_{12} will depend on the specific initial and final states. Nevertheless, we believe that a model based on interaction between states at very long range is required to explain the large rate constants for He in Table II. The calculations predict a dependence of the rate constants on temperature for Ne and Ar, whereas the rate constants for a curve crossing mechanism is only weakly dependent on temperature. Thus, measurement of rate constants vs temperature in Ne would be useful. The *ab initio* calculations of Hickman *et al.*[9] for the diabatic potentials for Xe($6p$) states with He indirectly support the idea of long range interactions because the degeneracy of the Ω components correlating to a given Xe($6p$) state begin to be removed even at 6 Å, the largest distance of the calculation.

The independence of the experimental rate constants on specific properties of the initial and final states (i.e., $6p'[1/2]_1\rightarrow 6d[5/2]_2$, $6p'[3/2]_1\rightarrow 7p[5/2]_2$, or $7p[3/2]_2\rightarrow 6d[3/2]_2$) is another fundamental reason to favor a model involving scattering of the Rydberg electron by He (or Ne). Two of the large cross sections even require change in the ion-core state of Xe^+. However, the Xe($6p'$ and $7p$) states have intrinsically (~15%) mixed $Xe^+(^2P_{1/2})$ and $Xe^+(^2P_{3/2})$ cores,[21] which seems sufficient to allow state-changing collisions between different Xe^+ core potentials. The Demkov formulation also can describe the cross section (~80 Å) for transfer by He collisions between the Kr($5p'[3/2]_2$) and Kr($5p'[1/2]_1$) states with a defect of 26 cm^{-1}. The rate constant is smaller than for Xe($6p',7p$) atoms because of the lower degree of Rydberg character of the Kr($5p$) atoms.

The calculated results shown in Fig. 14 may have some general significance for quenching of Xe* states by light molecular collision partners. Since the interaction exists at long range, Xe* states that have neighbors with small energy defects will become mixed during traversal of the entrance channel. Even though the final product states may be determined by shorter range interactions, the long range coupling among Xe* states with small energy defects may affect collision processes with molecules.

C. Comparison of Xe($6p',7p$) rate constants in Ar

Recommendations for the best experimental rate constants in Ar were made when the data were presented. The new cw data extend and generally agree with the results from pulsed experiments,[10] and product state assignments are partly known for quenching of some levels. One difference between relaxation of Xe($6p'$ and $7p$) states in Ar vs He is that Xe($7p[1/2]_1$), the lowest level in the $7p$ manifold, has a large rate constant in Ar for transfer to states (currently not assigned) in the Xe($7s$ or $5d$) manifolds. Thus, the Xe($6p',7p,6d$) concentrations cannot accumulate in the lowest five levels in Ar buffer gas, as it can in He or Ne. The explanation of this difference is straightforward. The $XeAr^+(X\ ^2\Sigma^+)$ state is bound by 0.18 eV.[9] Adding the $7p$ Rydberg electron will generate a bound XeAr* molecular state that correlates to Xe($7p[1/2]_1$). Thus, Ar+Xe($7p[1/2]_1$) collisions sample an attractive potential that can be crossed by repulsive diabatic potentials correlating to Xe($5d$) states. In contrast, the Ne–Xe($7p$) and He–Xe($7p$) potentials will not be bound and crossings are less likely.

The Hickman *et al.*[9] calculations were done for the Xe($6p$) and Xe($5d$) states interacting with Ar; however, some general features should apply to the $7p$ and $6d$ sets of levels. Thus, a brief comparison is worthwhile. As already mentioned, several of the lower Xe($7p$) states will correlate to XeAr* molecules with the bound $XeAr^+(X\ ^2\Sigma^+)$ core with

R_e=3.1 Å and D_e=0.18 eV.[9] Other ArXe($7p$) potentials have the $ArXe^+(A^2\Pi_{3/2})$ core with $R_e \approx 4$ Å and D_e=0.07 eV.[9] The Xe($6p'$) states correlate to ArXe* molecules with the $ArXe^+(B\ ^2\Pi_{1/2})$ core with $R_e \approx 3.8$ Å and D_e=0.11 eV.[9] These Ar+Xe($6p',7p$) potentials plus the additional Ar +Xe($6d$) potentials with different degrees of binding, all in a 0.17 eV range, will form a dense network of interactions. This network will give many ways to couple a given initial state to several final states, thus the total rate constants are very similar for all initial states and product states with large defects are possible. Hickman *et al.*[9] were able to identify the most important interactions and explain most of the state-to-state rate constants in term of coupling of diabatic potentials in the 76 000–84 000 cm^{-1} region for the Xe($6s',6p,5d$) levels. Such identifications may be impossible for the more dense network arising from the Xe($6p',7p,6d$) states. The predicted Demkov rate constants range from 1.0×10^{-10} $cm^3\ s^{-1}$ to 1.0×10^{-11} $cm^3\ s^{-1}$ for exit channels with energy defects of 20–45 cm^{-1}, respectively. For product channels with larger defects, coupling via the network of curve crossings will dominate the quenching mechanism.

V. CONCLUSIONS

State-to-state rate constants have been measured for several levels in the Kr($5p',4d$) and Xe($6p',7p,6d$) manifolds in the He and Ar buffer gases at 300 K. In addition to giving information about processes for specific individual states, these data provide an overall view of how energy passes through the 88 000–89 000 cm^{-1} range for Xe* and the 97 000–98 000 cm^{-1} range for Kr* in He and Ar buffer gases. The transfer rate out of the lower energy Xe($6p',7p$) levels is slow in He (and Ne) and relatively high Xe* concentrations can accumulate in these levels. However, the rates constants are larger in Ar (typically 2×10^{-10} $cm^3\ s^{-1}$) and the energy will be collisionally transferred to the Xe($7s,5d$) manifold. The lowest energy Kr($5p$) level has a large rate constant for transfer to the Kr($4d$) levels in both He and Ar, and the energy flow will be determined by the rate constants for the Kr($4d[1/2]_{0,1}$) states, which have not yet been determined.

The rate constants between pairs of Xe($6p',7p,6d$) states with small energy defects (<50 cm^{-1}) in He are exceptionally large, $10–20\times10^{-10}$ $cm^3\ s^{-1}$. Rate constants of this magnitude can be explained using the Demkov formulation for parallel entrance and exit potentials that interact via scattering of the Rydberg electron off the incoming He atom. The nominally different Xe^+ core states for the Xe($6p'$) vs Xe($7p$) or Xe($6d$) do not seriously restrict the coupling between pairs of initial and final states. The smaller rate constants ($0.1–1.0\times10^{-10}$ $cm^3\ s^{-1}$) with larger energy defects can be rationalized by more conventional diabatic curve crossing processes at short range. Understanding the fast collisional coupling rates between Xe* states in He is important for designing state specific experiments, such as the conversion of Xe($6s[3/2]_2$) atom concentration into a Xe($6s'[1/2]_0$) concentration via optical pumping utilizing levels in the Xe($6p'$ or $7p$) manifolds.

ACKNOWLEDGMENTS

This work was supported by the Petroleum Research Foundation (administered by the ACS) and by the National Science Foundation (CHE-9120489). We wish to thank Professor P. Hickman (Lehigh University) for providing his calculated potentials for Xe($6p,5d,6s'$) atoms interacting with He and for advice on how to evaluate the interaction energy between Xe($7p,6p'$) atoms with He, Ne, and Ar. We also thank Dongping Zhong for assistance with some of the cw experiments with Xe($7p$) states.

[1] D. P. Zhong and D. W. Setser, Chem. Phys. Lett. **207**, 555 (1993).
[2] Ch. K. Rhodes, *Topics in Applied Physics: Excimer Lasers* (Springer-Verlag, New York, 1984); W. L. Nighan and M. C. Fowler, IEEE J. Quantum Electron. **QE-25**, 791 (1989); W. L. Nighan, R. A. Sauerbrey, Y. Zhu, F. K. Tittel, and W. L. Wilson, Jr., IEEE J. Quantum Electron. **QE-23**, 253 (1982).
[3] (a) W. J. Alford, G. N. Hays, M. Ohwa, and M. J. Kushner, J. Appl. Phys. **69**, 1843 (1991); (b) M. J. Ohwa, T. Moratz, and M. J. Kushner, *ibid*. **66**, 5131 (1989); (c) W. J. Alford and G. N. Hays, *ibid*. **65**, 3760 (1989); (d) W. J. Alford, IEEE J. Quantum Electron. **26**, 1033 (1990); (e) O. V. Sereda, V. F. Tarasenko, A. V. Fedenev, and S. I. Yakovlenko, Quantum Electron. **23**(6), 459 (1993); (f) G. A. Hebener and G. N. Hays, J. Appl. Phys. **74**, 3673 (1993); (g) S. A. Lawton, J. B. Richards, L. A. Newman, L. Specht, and T. A. DeTemple, *ibid*. **50**, 3888 (1979).
[4] R. Hilbig and R. Wallenstein, IEEE J. Quantum Electron. **QE-19**, 194 (1983); J. W. Hepburn, Israel J. Chem. **24**, 273 (1984); N. B. DeRone and V. P. Krainov, *Fundamentals of Nonlinear Optics of Atomic Gases* (Wiley, New York, 1988); K. Miyazaki, H. Sakai, and T. Sata, Appl. Opt. **28**, 699 (1989); R. Hilbig and R. Wallenstein, IEEE J. Quantum Electron. **QE-17** 1566 (1981).
[5] R. Sobczynski, R. Beaman, D. W. Setser, and N. Sadeghi, Chem. Phys. Lett. **154**, 349, (1989); D. P. Zhong, D. W. Setser, W. Gadomski, and R. Sobczynski (unpublished); N. Sadeghi, I. Colomb, J. Stoyanova, D. W. Setser, and D. Zhong, J. Chem. Phys. **102**, 2744 (1995).
[6] J. Xu and D. W. Setser, *ibid*. **94**, 4243 (1991); **92**, 4191 (1990); J. K. Ku and D. W. Setser, ibid. **84**, 4304 (1986).
[7] (a) M. R. Bruce, W. B. Layne, C. A. Whitehead, and J. W. Keto, J. Chem. Phys. **92**, 2917 (1990); (b) N. Bowering, M. R. Bruce, and J. W. Keto, *ibid*. **84**, 709, 715 (1986); (c) C. A. Whitehead, H. Pounasr, M. R. Bruce, H. Cai, J. Kohel, W. B. Layne and J. W. Keto, ibid. **102**, 1965 (1995).
[8] W. J. Alford, J. Chem. Phys. **96**, 4330 (1992); this reference provides a summary of the Xe($6p$) relaxation rate constants in rare gases and radiative lifetimes.
[9] A. P. Hickman, D. L. Huestis, and R. P. Saxon, J. Chem. Phys. **96**, 2099 (1992); **98**, 5419 (1993).
[10] (a) G. Inoue, J. K. Ku, and D. W. Setser, J. Chem. Phys. **81**, 5760 (1984); (b) H. Horiguchi, R. S. F. Chang, and D. W. Setser, *ibid*. **75**, 1207 (1981).
[11] V. Alekseev and D. W. Setser, J. Phys. Chem. (in press).
[12] J. C. Miller, Phys. Rev. A **40**, 6969 (1989); M. B. Rankin, J. P. Davis, C. Giranda, and K. G. Bobb, Opt. Commun. **70**, 3451 (1989).
[13] R. Sobczynski and D. W. Setser, J. Chem. Phys. **95**, 3310 (1991).
[14] V. Hefter and K. Bergmann, in *Atomic and Molecular Beam Methods, Vol. 1*, edited by G. Scoles (Oxford University Press, New York, 1988).
[15] M. Aymar and M. Coulombe, Atomic Data Nucl. Data Tables **21(6)**, 538 (1978).
[16] R. Bulsrisch and J. Stoer, Numer. Mathemat. **8**, 1 (1966).
[17] R. S. F. Chang, H. Horiguchi, and D. W. Setser, J. Chem. Phys. **73**, 778 (1980).
[18] L. G. Piper, D. W. Setser, and M. A. A. Clyne, J. Chem. Phys. **63**, 5018 (1975); T. O. Dreiling and N. Sadeghi, J. Phys. **44**, 1007 (1983); M. S. de Vries, V. I. Srdanov, G. W. Tyndal, and R. M. Martin, Chem. Phys. Lett.

114, 233 (1985); E. R. T. Kerstel, C. P. J. W. Van Kruysdijk, J. C. Vlugter, and H. C. W. Beijerinck, Chem. Phys. **121**, 211 (1988).
[19] Y. N. Demkov, Sov. Phys.—JETP **18**, 138 (1964).
[20] (a) A. P. Hickman, Phys. Rev. A **23**, 87, (1981); (b) R. K. Janev, J. Phys. B **4**, 215, (1971); (c) B. M. Smirnov, Sov. Phys.—JETP **24**, 314 (1967); (d) R. E. Olson, Phys. Rev. A **15**, 631 (1977); (e) T. F. Gallagher and W. E. Cooke, *ibid*. **19**, 820 (1979); **19**, 2161 (1979); (f) T. F. Gallagher, S. A. Edelstein, and R. M. Hill, *ibid*. **15**, 1945 (1977).
[21] S. Liberman, J. Phys. **30**, 53 (1969). M. C. Coulombe and J. Sinzelle, J. Phys. **36**, 774 (1975).